PIER C

Hybrid Method for Electromagnetic Vibration Calculation of Flatted Single-Layer Interior Permanent Magnet Synchronous Machines for Flywheel Application

Xinjiang Jiang, Lei Zhang, Fuwang Li, and Sai Zhang*

Shanxi Energy Internet Research Institute, China

ABSTRACT: In this paper, a hybrid method is proposed for electromagnetic vibration prediction of flatted single-layer interior permanent magnet synchronous machines (IPMSMs) for flywheel application. The proposed hybrid model combines the mesh-based equivalent magnetic network (EMN) model and vibration transfer function method. A small size 4-pole/6-slot flatted single-layer IPMSM for demonstration purposes is manufactured to illustrate the proposed hybrid method. Firstly, the modeling method of the proposed mesh-based EMN model is introduced, and the electromagnetic forces are calculated. Second, the vibration transfer function construction method is introduced. Thirdly, the modal superposition method is applied to compute the electromagnetic vibration acceleration of the 4-pole/6-slot IPMSM. Finally, the simulation and experimental test at rated rotational speed condition are used to verify the effectiveness of the proposed hybrid method, and the vibration acceleration at twice the fundamental frequency from proposed method has the acceptable agreement with tested and simulation. The proposed method can be applied to predict the electromagnetic vibration for flatted single-layer IPMSM with concentrated winding at different operating conditions.

1. INTRODUCTION

In recent years, flywheel energy storage systems have received significant attention due to the development of green energy [1]. Interior permanent magnet synchronous machines (IPMSMs) can be used in the flywheel energy storage systems due to their wide speed operation range and high-power density [2]. The drive motors of flywheel energy storage systems typically operate at very high rotational speeds, making it essential to minimize the vibration amplitude of the drive motors as much as possible. The main source of vibration in IPMSMs is electromagnetic vibration caused by electromagnetic forces. The multi-physis finite element method (FEM) is commonly used to evaluate the vibration performance of motors [3]. However, FEM requires extensive meshing, resulting in low computational efficiency and long computation times. Therefore, the research on fast methods for calculating electromagnetic vibrations of IPMSMs is essential.

To calculate the vibration of an IPMSM, first it is necessary to compute the electromagnetic force harmonics, which entails calculating the magnetic field within the motor. Currently, there are various methods for calculating the internal magnetic field of motors, such as FEM, analytical methods, subdomain models, and equivalent magnetic network (EMN) methods. The widely used FEM employs meshing to discretize the partial differential equations throughout the motor, offering high computational accuracy but at the cost of long computation times [4]. Analytical methods and subdomain models are often suitable for motors with simpler geometries but struggle

to account for saturation in the core regions [5]. In recent years, the EMN method has received considerable attention and has been validated for application in various types of motors, including IPMSMs, vernier motors, and linear motors, due to its fast computation speed. Therefore, this paper employs a partitioned EMN method to model the IPMSM and calculate the magnetic flux density in the air-gap region to obtain the electromagnetic forces acting on the stator teeth.

To ensure computational accuracy, FEM is often used to calculate the vibration response of motors. However, commercial FEM software can be prohibitively expensive, and the accuracy of the calculations is directly related to the mesh resolution. Therefore, to reduce computational costs and enhance efficiency, many researchers employ the vibration transfer function method based on modal superposition to achieve rapid computation of motor vibrations. In [6], the vibration transfer function of a 10-pole/12-slot electrical machine is derived by using FEM, and the force modulation and tangential effects were considered. The results show that this method has high precision and high efficiency for electromagnetic force computation. In [7], an analytical method was proposed to obtain the vibration transfer function and had good agreement with the experimental test. Therefore, the vibration transfer function method is an effective and fast method to compute the vibration acceleration of electrical motor.

This article proposes an improved EMN model for flatted single-layer IPMSM and combined with the vibration transfer function to predict the vibration performance. The structure of this paper is as follows. In Section 3, the proposed improved

---

* Corresponding author: Sai Zhang (saizhang1977@gmail.com).
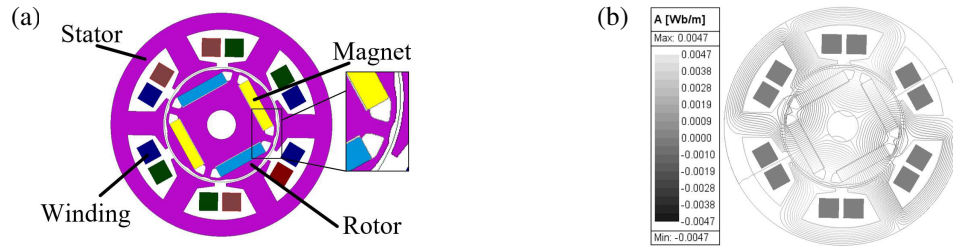
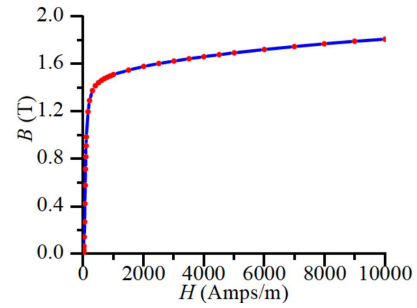**FIGURE 1**. The 4-pole/6-slot flatted single-layer IPMSM. (a) 2-D model. (b) Flux line distribution.

mashed-based EMN mode for 4-pole/6-slot flatted single-layer IPMSM will be introduced. The magnetic flux density and electromagnetic force in air-gap will be calculated and compared with FEM in this section. In Section 4, the modal parameters and vibration transfer function of the 4-pole/6-slot flatted single-layer IPMSM will be constructed, and the proposed hybrid electromagnetic vibration computation method will be validated by FEM and experimental test. The conclusion will be given in Section 5. The contribution of this paper can be summarized as (1) Proposing an improved EMN modeling method for flatted single-layer IPMSM with notched rotor surface using hybrid permeance element. (2) Combining the EMN model and vibration transfer function to calculate the vibration response for flatted single-layer IPMSM. The proposed method can be applied to predict the electromagnetic force and vibration for flatted single-layer IPMSM with concentrated winding at different operating conditions. The simulated and experimental results demonstrate that the proposed method has acceptable accuracy.

2. EMN MODEL OF THE IPMSMS

The electromagnetic forces on the stator teeth of the machine can be obtained using the Maxwell stress tensor method by calculating the radial and tangential components of the magnetic flux density in the air-gap. The mesh-based EMN model is applied to obtain the flux density in the air-gap of the machine. The proposed model of the small size 4-pole/6-slot flatted IPMSM used for verification in this article is shown in Fig. 1(a), and the flux line distribution of this machine is shown in Fig. 1(b). In flywheel energy storage applications, the flywheel typically operates at extremely high rotational speeds to store more kinetic energy. Therefore, the drive motor must support high-speed operation. This flatted single-layer IPMSM uses a 2-pole pair design to reduce motor losses at high speeds, and with this rotor structure, it can mitigate the effects of centrifugal force on the permanent magnets to some extent without the need for a rotor sleeve. The detailed information about the 4-pole/6-slot flatted IPMSM is summarized in Table 1. The B-H curve of core region is shown in Fig. 2.

2.1. EMN Model in Stator Region

Figure 3 shows the EMN model of each part of the stator region. From Fig. 1(a), the 4-pole/6-slot flatted single-layer IPMSM has three-phases double-layer concentrated winding. Therefore, the equivalent magnetic potential generated by windings

FIGURE 2. B-H data of B35AH230.

**TABLE 1**. Detailed parameters of 4-pole/6-slot flatted single-layer IPMSM.

Quantity	Value (Unit)
Slot number	6
Pole pairs	2
Stator outer radius	18 mm
Stator inner radius	10 mm
Rotor outer radius	9.5 mm
Rotor inner radius	2.5 mm
Stack length	20 mm
Air-gap length	0.5 mm
Magnet width	8.8 mm
Magnet length	1.9 mm
Magnet material	N45UH
Remanence	1.36T
Core material	B35AH230
Rotational speed	32000 r/min

can be equivalent as a source in the EMN at the stator tooth body. The equivalent magnetic potential sources F_w can be calculated as follows [8]:

$$F_w = N_c I_w \sin\left(2\pi f_e t + \theta_w\right) \qquad (1)$$

where $w = 1, 2, 3$ represents phases A, B, and C, respectively; N_c is the number of turns; I_w is the current amplitude of phase w; f_e and θ_w are frequency and phase angle of the phase current, respectively; and t is the time.

The stator yoke region between two stator teeth modeled by two permeances P_{yoke} due to the distribution of flux lines is relatively uniform as shown in Fig. 1(b), which can be expressed
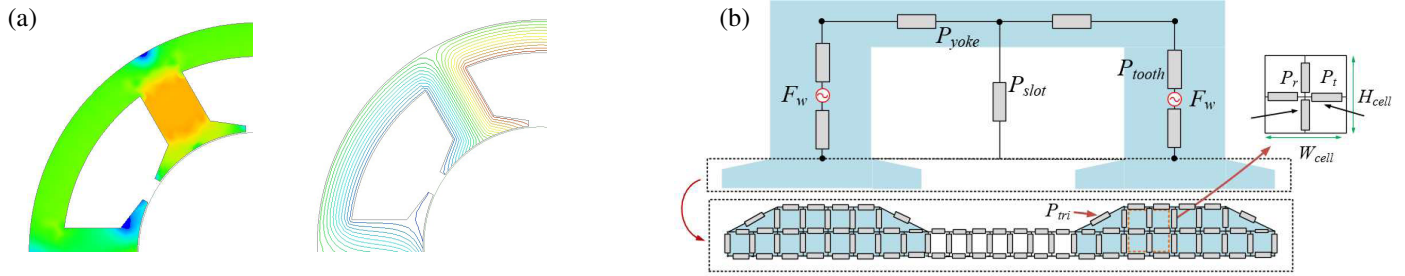
FIGURE 3. Magnetic state and EMN model of stator core and winding region. (a) Magnetic state. (b) EMN model.
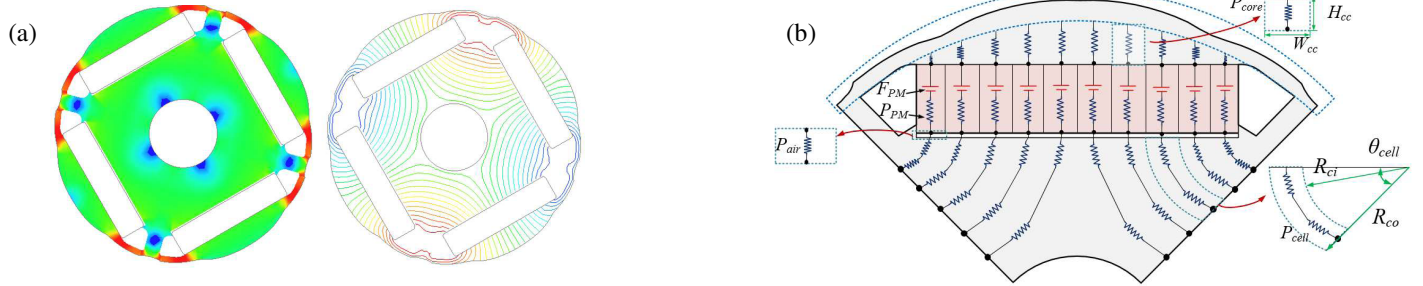
FIGURE 4. Magnetic state and EMN model of the first part of rotor core. (a) Magnetic state. (b) EMN model.

as [8, 9]:

$$P_{yoke} = \frac{2\mu_0\mu_r L_{stack}}{\theta_{yoke}} \ln\frac{R_o}{R_i} \qquad (2)$$

where μ and μ_r are vacuum permeability and relative permeability, respectively; L_{stack} is the axial length of stator core; R_o and R_i are the outer radius and inner radius of the stator yoke; θ_{yoke} is the arc length between two adjacent stator teeth.

Similarly, each stator tooth can be modeled by two radially arranged permeances P_{tooth}, which can be obtained as follows:

$$P_{tooth} = 2\mu_0\mu_r L_{stack}\frac{W_t}{H_s} \qquad (3)$$

where W_t and H_s are the width and height of stator tooth body, respectively.

As shown in Fig. 1(b), there is a certain amount of leakage flux in the stator slot. To account for the impact of leakage flux on electromagnetic performance, a permeance P_{slot} is added at the slot region to simulate the path of the leakage flux, which can be expressed as:

$$P_{slot} \approx \mu_0\mu_r L_{stack}\frac{W_s}{H_s} \qquad (4)$$

where W_s is the average width of stator slot region.

Due to the complex distribution of magnetic field at the stator tooth tips and slot openings, a rectangular permeance element is used to model this region, as shown in Fig. 3. There exist two radial and two tangential permeances in one rectangular permeance element to model the pole shoe and slot opening at the stator core region, which can be expressed as follows:

$$P_r = 2\mu_0\mu_r L_{stack}\frac{W_{cell}}{H_{cell}} \qquad (5)$$

$$P_t = 2\mu_0\mu_r L_{stack}\frac{H_{cell}}{W_{cell}} \qquad (6)$$

where H_{cell} and W_{cell} are the height and weight of the rectangular permeance element, respectively. The permeance P_{tri} used for modeling the the bevel area of the pole shoe can be obtained through [8]:

2.2. EMN Model in Rotor and Air-Gap Region

The rotor core surface of this 4-pole/6-slot flatted single-layer IPMSM has undergone irregular shaping treatment to minimize the torque ripple, resulting in a nonuniform air-gap region. This non-uniformity presents significant challenges for modeling using the EMN model. Consequently, this study employs a discretized modeling approach to address the irregular air-gap area.

Figures 4 and 5 show the proposed EMN model for rotor core and air-gap region. The rotor and air-gap region of the 4-pole/6-slot flatted single-layer IPMSM are divided into two parts for EMN modeling. The first part comprises the rotor core and permanent magnet (PM) region, while the second part encompasses the air-gap region and the surface area of the rotor core.

Firstly, the PM section is modeled using multiple rectangular units of the same width. Each rectangular unit incorporates a PM MMF source FPM and a permeance PPM, which can be expressed as:

$$\begin{cases} F_{PM} = \frac{B_{rm}h_{PM}}{\mu_0} \\ P_{PM} = \mu_0\frac{w_{PM}L_{stack}}{N_{PM}h_{PM}} \end{cases} \qquad (7)$$
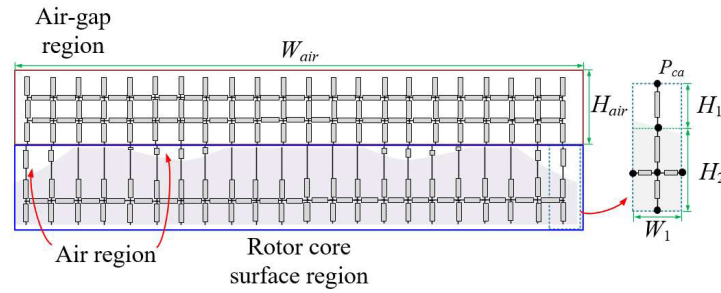
FIGURE 5. EMN model of the second part of rotor core and air-gap.

where B_{rm} is the residual magnetic density; h_{PM} and w_{PM} are the height and weight of PM; N_{PM} is the number of rectangular units.

Second, the rotor core region above the PM is modeled using several rectangular units with varying heights. As the flux lines in this region are predominantly perpendicular to the PM, each unit incorporates only a single permeance P_{core}, which can be expressed as:

$$P_{core} = \mu_o \mu_r L_{stack} \frac{W_{cc}}{H_{cc}} \quad (8)$$

where W_{cc} is the width of rectangular unit, which is equal to w_{PM}/N_{PM}, and H_{cc} is the height of rectangular unit. It is important to emphasize that the air region beneath each unit of the PM need be modeled using permeance P_t, with its calculation method like that of permeance P_{PM} of PM.

Third, as illustrated in Fig. 1(b), the flux lines in the rotor core region beneath the PM region exhibit an arc-shaped distribution. Consequently, this region can be modeled using multiple arc-shaped path units. Each arc-shaped unit includes two permeances P_{cell}, which can be obtained as follows:

$$P_{cell} = \frac{2\mu_0 \mu_r L_{stack}}{\theta_{cell}} \ln \frac{R_{co}}{R_{ci}} \quad (9)$$

where R_{co} and R_{ci} are the outer radius and inner radius of the arc-shaped unit, and θ_{cell} is the arc length of the arc-shaped unit.

For the modeling method of the second part, it mainly includes a regular air-gap region and an irregular rotor core surface region. The same EMN modeling method as used for the stator tooth pole shoe is applied in the air-gap region to facilitate the subsequent calculation of the radial and tangential flux densities in the air gap. The calculation method of these permeance is the same as in (5) and (6). As shown in Fig. 4, the permeance P_{PM} of the permanent magnet region is connected to the permeance P_{core} above it and the permeance P_{air} below it. All the permeances in this part will be applied in the total permeance matrix **G** (Eq. (11)) based on their connection relationship.

For the rotor core surface region, which includes both core and air and has an irregular shape, multiple rectangular units are used for modeling this region. If a rectangular unit only contains core, it is modeled using four permeances, the same as in (5) and (6). If the rectangular unit contains both air and

core, the air region is equivalently modeled using one permeance P_{ca}, while the core region is modeled using the same four permeances as previously described. The permeance P_{ca} can be expressed as:

$$P_{ca} = \mu_0 L_{stack} \frac{W_1}{H_1} \quad (10)$$

where W_1 is the width of the rectangular unit, and H_1 is the height of the rectangular unit in air region.

2.3. Computation of Electromagnetic Force Density

After establishing the EMN model of the 4-pole/6-slot flatted single-layer IPMSM as described above, the entire EMN model can be solved. This allows for the determination of the radial and tangential flux densities in the air-gap region, which are then used to calculate the electromagnetic force density. The solution of the EMN model is based on Kirchhoff's law, which establishes the relationship among MMF matrix **F**, magnetic permeance matrix **P**, and magnetic flux matrix Φ as:

$$\mathbf{F}_{n \times n} = \mathbf{P}_{n \times n}^{-1} \mathbf{\Phi}_{n \times 1} \quad (11)$$

where n is the number of permeance in the whole EMN model [10]. Based on the complete nodal voltage matrix in (11), a successive over-relaxation method is utilized to solve the proposed linear matrix equation. This approach is derived from an enhanced Gauss iterative method, making it highly effective for handling higher-order equations. The magnetic flux density $B(i, j)$ between two nodes i and j at each permeability can be calculated from [9]:

$$B(i, j) = \frac{F(i) - F(j)}{S(i, j)} P(i, j) \quad (12)$$

where S is the cross-sectional area of the permeance $P(i, j)$. Due to the nonlinear characteristic of the permeance in the iron core region, it is necessary to iteratively update the permeability in each calculation step. The iteration process should be terminated and proceeds to the next step when the following equation is satisfied:

$$\max \left| B^{(k)}(i, j) - B^{(k+1)}(i, j) \right| < \zeta \quad (13)$$

where ξ is the deviation limit as 1×10^{-3}.

The magnetic flux density in air-gap region can be obtained after accomplishing the EMN model solution. Therefore, based

on the Maxwell tensor method, the radial and tangential electromagnetic force densities can be acquired through solving magnetic flux density as [11]:

$$f_r = \frac{1}{2\mu_0}\left(B_n^2 - B_t^2\right) \tag{14}$$

$$f_t = \frac{1}{2\mu_0}B_n B_t \tag{15}$$

where B_n and B_t are the radial and tangential magnetic flux densities in air gap, respectively, as shown in Fig. 6. The tangential force mainly generates the electromagnetic torque of the motor, and the radial force is the main source to generate the electromagnetic vibration. The radial force is the main research object, and tangential force is neglected in this paper.
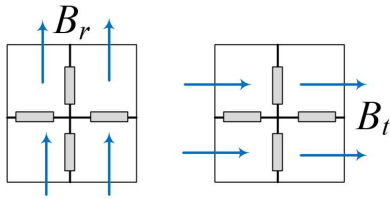

FIGURE 6. Calculation of radial and tangential force densities.

Figures 7(a) and 7(b) show the radial magnetic flux and harmonics results from FEM and proposed EMN model, respectively. The radial air-gap magnetic flux density waveforms calculated using the proposed method demonstrate a significant degree of consistency with the results obtained through FEM. The computation times for the FEM and proposed EMN model are 132s and 37s, respectively. However, the computational error of the radial magnetic flux density waveform occurs in the stator slot opening area. To further enhance the computational accuracy, one can increase both the number of layers and the quantity of permeances in the slot opening region.

Figures 8(a) and 8(b) show the waveforms and harmonic results of radial electromagnetic force density between the FEM and proposed FEM model. It can be observed that the fundamental component of the radial electromagnetic force density is the 4th order, with a computational error of 3.5%. However, the calculation errors for higher-order electromagnetic force harmonics, specifically the 6th, 8th, 10th, and 12th orders, are significantly larger, at 14.5%, 13.8%, 15.2%, and 12.2%, respectively. In addition, Table 2 shows the comparisons of the amplitude of the 2$^{\text{nd}}$-order radial flux density between simulation and EMN at different load conditions, which shows a good agreement between simulation and proposed EMN method.

TABLE 2. Comparisons of the amplitude of the 2nd-order radial flux density between simulation and EMN at different load condition.

Speed (r/min)	Load (N.m)	Simulation (T)	EMN (T)
32000		0.792	0.776
32000	0.125	0.893	0.889
22000	0.064	0.813	0.798
12000	0.113	0.824	0.809

3. CONSTRUCTION OF VIBRATION TRANSFER FUNCTION

3.1. Computation of Electromagnetic Force Density

The electromagnetic force density obtained through the proposed EMN model in the previous section is typically applied as a concentrated force load in analytical calculations or FEM. According to the force transmission model (Fig. 9), the concentrated force acting on the center of each stator tooth can be expressed as:

$$F_{n,z}\left(\theta,t\right) = \int_{-\frac{1}{2}\theta_s + \frac{2\pi}{Q_s}z}^{\frac{1}{2}\theta_s + \frac{2\pi}{Q_s}z} f_r\left(\theta,t\right) R_{si}L_{stack}d\theta \tag{16}$$

where Q_s is the number of stator slot, θ_s the angular span of the stator tooth tip, z the zth stator tooth, and R_{si} the stator inner radius. Furthermore, the concentrated force is typically decomposed into the frequency domain using Fast Fourier Transform (FFT) method for analysis, and subsequently modal superposition method is utilized to calculate the vibration in the frequency domain, which can be expressed as:

$$\begin{cases} F_{n,z}\left(\theta\right) = \sum_v a_v \cos\left(n\theta + \varphi_v\right) \\ a_v = \frac{2}{v\pi}F_z\sin\frac{\alpha\pi}{Q_s}v \end{cases} \tag{17}$$

where F_z represents the amplitude of the concentrated force acting on the zth stator tooth surface, α the ratio of tooth width to tooth pitch, θ the mechanical angle, v harmonic order, and φ_v the phase angle.

3.2. Computation of Vibration Transfer Function

In experimental testing, vibration acceleration sensors are commonly employed to measure the vibration acceleration on the surface of the motor stator or housing, as illustrated in Fig. 10. For instance, the vibration transfer function represents the mapping relationship between the vibration response V_1 of the motor surface and the radial electromagnetic forces $F_{n,1}$, $F_{n,2}$, $F_{n,3}$, ...F_{nQ_s} acting on the stator tooth face. The transfer function between force $F_{n,j}$ and the vibration at point i can be expressed as [7, 12] and as shown in Fig. 11:

$$H_{ij} = \frac{a_0\omega_{fv}^2 R_o R_{my}}{Eh_y}\frac{1}{\sqrt{\left[1-\left(\frac{\omega_{fv}}{\omega_0}\right)^2\right]^2 + \left[2\varsigma_0\frac{\omega_{fv}}{\omega_0}\right]^2}}$$

$$+ \sum_v \frac{12a_v\omega_{fv}^2 R_o R_{my}^3}{E\left(v^2-1\right)h_y^3}\frac{1}{\sqrt{\left[1-\left(\frac{\omega_{fv}}{\omega_v}\right)^2\right]^2 + \left[2\varsigma_v\frac{\omega_{fv}}{\omega_v}\right]^2}}$$

$$\cos v\left[\theta_i - \left(j-1\right)2\pi/Q_s\right] \tag{18}$$

where R_{my} is the average radius of the stator yoke, E the Young's modulus of the stator, h_y the thickness of stator yoke, ω_{fv} the angular velocity of the vth order force, ω_v the angular velocity of the vth order modal shaper of stator, and ς_v the vth order modal ratio, which can be obtained through [12]:
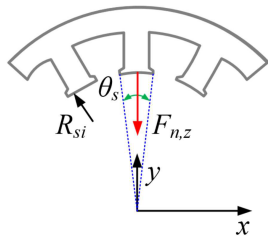
$$\varsigma_v = \frac{1}{2\pi}\left(2.76\times10^{-5}\omega_v + 0.062\right) \tag{19}$$
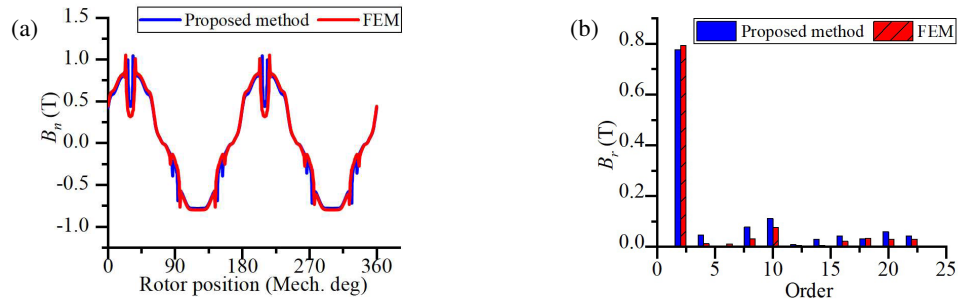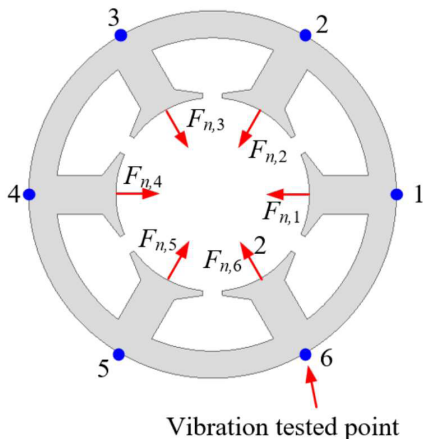
FIGURE 7. Comparison of radial magnetic flux density waveform and harmonics between FEM and proposed EMN model.
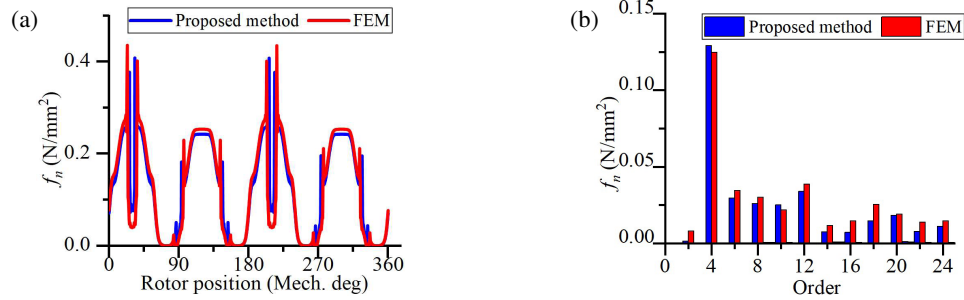
FIGURE 8. Comparison of electromagnetic force between FEM and proposed EMN model. (a) Waveforms. (b) Harmonics results.
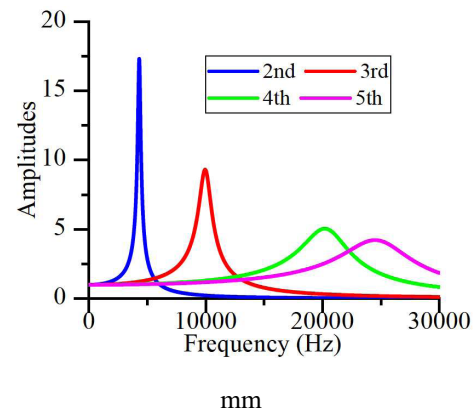

FIGURE 9. Force transfer model.

FIGURE 11. Transfer function.

FIGURE 10. Vibration tested point position for vibration transfer function.

3.3. Vibration Synthesis

The vibration acceleration of the point i in the stator surface can be synthesized by vibration transfer function and radial concen-

trated force, which can be derived as:

$$V_i = \sum_{j=1}^{Q_s} H_{ij} F_{n,j} \qquad (20)$$

Then, the total vibration acceleration of the stator outer surface can be obtained through the superposition principle, which can be expressed as:

$$
\begin{bmatrix} A_1 \\ A_2 \\ A_3 \\ \vdots \\ A_{Q_s} \end{bmatrix} = \begin{bmatrix} H_{11} & H_{12} & H_{13} & \cdots & H_{1Q_s} \\ H_{21} & H_{22} & & & \\ H_{31} & & \ddots & & \vdots \\ \vdots & & & H_{ij} & \\ H_{Q_s 1} & & \cdots & & H_{Q_s Q_s} \end{bmatrix} \begin{bmatrix} F_{n,1} \\ F_{n,2} \\ F_{n,3} \\ \vdots \\ F_{n,Q_s} \end{bmatrix}
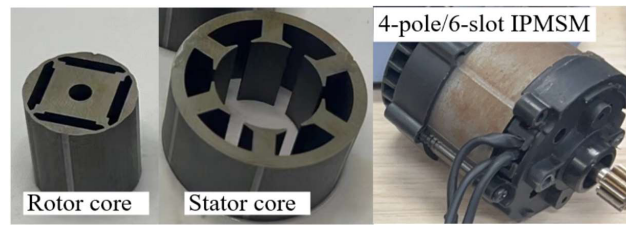$$

$$(21)$$

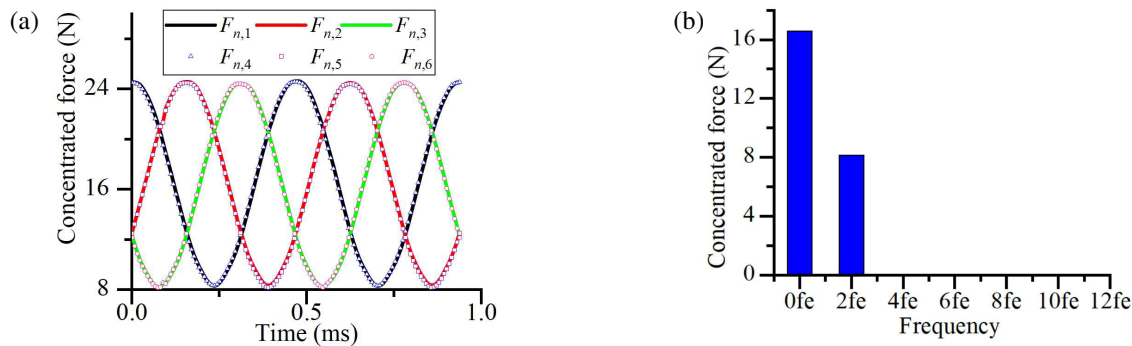**FIGURE 12**. Experimental 4-pole/6-slot flatted single-layer IPMSM.

FIGURE 13. Concentrated force of 4-pole/6-slot flatted single-layer IPMSM. (a) Waveforms varying times. (b) FFT results of $F_{n,1}$.

4. VIBRATION VALIDATION

A small size 4-pole/6-slot flatted single-layer IPMSM for demonstration purposes is manufactured to validate the proposed method, and the rotor core, stator core, and assembly machine are as shown in Fig. 12.

4.1. Modal Parameters

From (18), the modal frequency of each modal shape for stator core should be obtained, to calculate the vibration transfer function. The experimental test, FEM, and analytical method are used to acquire the modal frequency, summarized in Table 3.

TABLE 3. Modal parameters of stator.

Order	Modal	Order	Modal
2		3	
Analytical	4325.1 Hz	Analytical	9987.3 Hz
FEM	4459.7 Hz	FEM	10318.1 Hz
4		5	
Analytical	20391.2 Hz	Analytical	24845.6 Hz
FEM	19428.3 Hz	FEM	25215.3 Hz

4.2. Vibration Acceleration of 4-Pole/6-Slot IPMSM

Before calculating the vibration acceleration of the 4-pole/6-slot IPMSM, the radial concentrated forces acting on each stator tooth should be computed based on the electromagnetic force density from the proposed EMN model and using (16).

Fig. 13(a) and Fig. 13(b) show the waveforms of radial concentrated force acting on each tooth and the FFT results of $F_{n,1}$ at 32000r/min, respectively, where f_e is the fundamental electrical frequency of 4-pole/6-slot IPMSM. Fig. 14 shows the FFT results of the whole concentrated force at 32000r/min. The main components of the radial concentrated force are the (0th, $0f_e$) and (2nd, $2f_e$). Thus, the (2nd, $2f_e$) concentrated force has the main contribution to the vibration, which will cause the 2nd vibration mode.
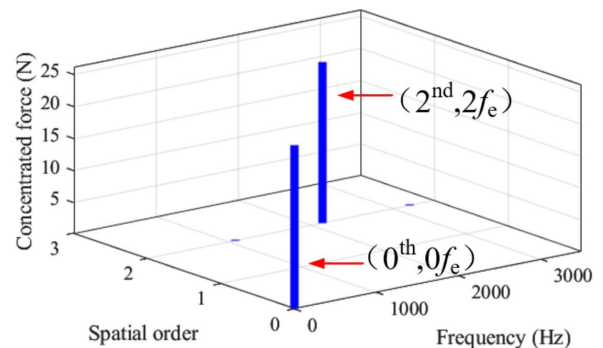

FIGURE 14. FFT results of whole concentrated force acting on each stator tooth surface.

Therefore, the vibration acceleration of the IPMSM can be obtained through submitting the calculated concentrated force from proposed EMN model to the vibration transfer function. Fig. 15 shows the vibration acceleration comparison among experimental test, FEM, and proposed method. It is evident that the maximum vibration acceleration of the 4-pole/6-slot IPMSM occurs at $2f_e$. At $2f_e$, the discrepancy of the vibration acceleration between the proposed method and the experimental test is 12.3%. The vibration acceleration amplitudes at $2f_e$
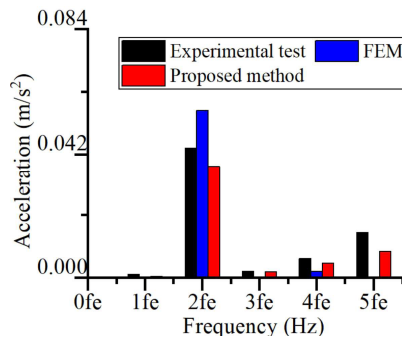
FIGURE 15. Vibration acceleration comparison among experimental test, FEM, and proposed hybrid method.

are $0.0387 \, \text{m/s}^2$ and $0.0435 \, \text{m/s}^2$ for the proposed method and the experimental test, respectively. The actual constraints and materials physical properties of the machine contribute to the presence of calculation errors. Additionally, during no-load experiments, a certain amplitude of current in the armature windings generates an armature magnetic field, which also leads to discrepancies in the vibration calculation results. Nevertheless, the overall accuracy of the proposed hybrid method remains within an acceptable range. Comparative analysis of the results verifies the accuracy of the EMN model in calculating electromagnetic forces within the proposed hybrid method.

5. CONCLUSION

This paper presents a hybrid method based on EMN model and vibration transfer function to calculate the electromagnetic vibration acceleration on the surface of a 4-pole/6-slot flatted single-layer IPMSM for flywheel application. The electromagnetic force density calculated from the proposed EMN model and FEM has a good agreement. The fundamental component of the radial electromagnetic force density is the 4th order, with a computational error of 3.5%. The vibration transfer function obtained through analytical method has a good accuracy and high efficiency to compute the vibration acceleration of the 4-pole/6-slot flatted single-layer IPMSM. This has been confirmed by both FEM simulation and experimental test. The vibration acceleration amplitudes at $2f_e$ are $0.0387 \, \text{m/s}^2$ and $0.0435 \, \text{m/s}^2$ for the proposed method and the experimental test, respectively, and the error is 12.3%. The advantage of the proposed method is its ability to provide a relatively fast assessment of motor vibration response and to quickly analyze the impact trends of motor dimensional parameters on vibration. However, its limitation lies in the need to further consider factors such as windings and the housing in constructing the vibration transfer function to improve calculation accuracy.

The hybrid method proposed in this paper can be applied to the flatted single-layer IPMSM with different dimensions or any slot-pole combinations.

REFERENCES

[1] Gao, M., Z. Yu, W. Jiao, W. Hu, H. Geng, Y. Liu, S. Liu, and Y. Liu, "Study on electromagnetic performance of permanent magnet rotor and dual stator starter generator for electric vehicle range extender," *Progress In Electromagnetics Research B*, Vol. 106, 39–55, 2024.

[2] Ghadamyari, M. A., M. Moallem, and B. Fahimi, "Improving the torque characteristics of interior PM synchronous motor using an asymmetric on-off method on the rotor surface," *Progress In Electromagnetics Research M*, Vol. 54, 55–65, 2017.

[3] Lee, S.-H., I.-J. Yang, W.-H. Kim, and I.-S. Jang, "Electromagnetic vibration-prediction process in interior permanent magnet synchronous motors using an air gap relative permeance formula," *IEEE Access*, Vol. 9, 29 270–29 278, 2021.

[4] Deng, W. and S. Zuo, "Electromagnetic vibration and noise of the permanent-magnet synchronous motors for electric vehicles: An overview," *IEEE Transactions on Transportation Electrification*, Vol. 5, No. 1, 59–70, 2019.

[5] Mendoncca, G. A., T. A. C. Maia, and B. d. J. C. Filho, "Improved semi-analytical magnetic field solution for high-speed permanent-magnet machines with permeable retaining sleeve including diffusion effect," *Progress In Electromagnetics Research B*, Vol. 88, 97–118, 2020.

[6] Fang, H., D. Li, J. Guo, Y. Xu, and R. Qu, "Hybrid model for electromagnetic vibration synthesis of electrical machines considering tooth modulation and tangential effects," *IEEE Transactions on Industrial Electronics*, Vol. 68, No. 8, 7284–7293, 2021.

[7] Hong, J., S. Wang, Y. Sun, and H. Cao, "A high-precision analytical method for vibration calculation of slotted motor based on tooth modeling," *IEEE Transactions on Industry Applications*, Vol. 57, No. 4, 3678–3686, 2021.

[8] Ghods, M., J. Faiz, M. A. Bazrafshan, H. Gorginpour, and M. S. Toulabi, "Design of an l-shaped array vernier permanent magnet machine for unmanned aerial vehicle propulsion using a schwarz-christoffel mapping-based equivalent magnetic network model," *IEEE Transactions on Industrial Electronics*, Vol. 71, No. 1, 237–249, 2024.

[9] Liu, G., S. Jiang, W. Zhao, and Q. Chen, "A new modeling approach for permanent magnet vernier machine with modulation effect consideration," *IEEE Transactions on Magnetics*, Vol. 53, No. 1, 1–12, 2017.

[10] Xiang, Q. W., M. Fang, Y. Yuan, and Y. Yu, "A novel hybrid excitation double-stator bearingless switched reluctance motor," *Progress In Electromagnetics Research M*, Vol. 69, 37–49, 2018.

[11] Kim, J.-H., S.-H. Park, J.-Y. Ryu, and M.-S. Lim, "Comparative study of vibration on 10-pole 12-slot and 14-pole 12-slot PMSM considering tooth modulation effect," *IEEE Transactions on Industrial Electronics*, Vol. 70, No. 4, 4007–4017, 2023.

[12] Shubov, I., "Noise and vibration of electrical machines," *Leningrad: Energoatomizdat*, Vol. 208, 1986.

[13] Gieras, J. F., C. Wang, and J. C. Lai, *Noise of Polyphase Electric Motors*, CRC press, 2018.